Volume 20
Number 2
14 January 2024
Pages 269–452

Soft Matter

rsc.li/soft-matter-journal

ISSN 1744-6848

ROYAL SOCIETY OF CHEMISTRY

PAPER
Yao Li *et al.*
Self-assembly of colloids with competing interactions confined in spheres

Soft Matter

PAPER

Cite this: *Soft Matter*, 2024, **20**, 304

Self-assembly of colloids with competing interactions confined in spheres

Ningyi Li,† Junhong Li,† Lijingting Qing, Shicheng Ma, Yao Li * and Baohui Li

Received 14th September 2023,
Accepted 17th November 2023

DOI: 10.1039/d3sm01227a

rsc.li/soft-matter-journal

At low temperatures, colloidal particles with short-range attractive and long-range repulsive interactions can form various periodic microphases in bulk. In this paper, we investigate the self-assembly behaviour of colloids with competing interactions under spherical confinement by conducting molecular dynamics simulations. We find that the cluster, mixture, cylindrical, perforated lamellar and lamellar structures can be obtained, but the details of the ordered structures are different from those in bulk systems. Interestingly, the system tends to form more perforated structures when confined in smaller spheres. The mechanism behind this phenomenon is driven by the relationship between the energy of the ordered structures and the bending of the confinement wall, which is different from the mechanism in copolymer systems.

I. Introduction

Self-assembly is a ubiquitous process in which multiple subunits spontaneously organise into collective and coherent structures or patterns. It plays an important role in both non-living and living systems, including polymers, colloids, liquid crystals, biomembranes, and proteins.[1,2] Applications of self-assembly include nanotechnology and nanostructure production in polymer systems and colloidal systems.[3–5]

Colloids with short-range attractive and long-range repulsive (SALR) interactions have attracted research interest in recent years. Previous studies have shown how the attractive and repulsive interactions of these colloids can be controlled experimentally, by precisely controlling the parameters of colloidal suspensions[6,7] and very recently dynamic control over the interparticle interactions by adding magnetic nanoparticles together with external magnetic fields.[8,9] The framework of competing interactions also applies to proteins, amphiphiles and other systems.[7,10–15] Studies of the self-assembly of colloids with SALR interactions suggest that short-range interparticle attraction is frustrated by long-range repulsion, preventing particles from merging and thus leading such systems to microphase separation and forming ordered phases at low temperatures, including cluster phase, cylindrical phase, lamellar phase, and others.[16–19] These phases are also observed in bulk diblock copolymer systems.[20–26] The remarkable similarity between the bulk phase diagram of colloids with SALR interactions and that of diblock copolymers has been confirmed by computer simulations[17] and a Landau–Brazovskii model has been proposed to explain it.[27]

Self-assembly under confinement often leads to richer patterns and structures.[28–30] The self-assembly of diblock copolymers under various confinements has been extensively studied,[30–46] among which it is shown that helical morphologies are observed in systems confined in cylindrical pores with neutral surfaces.[30,47–49] Meanwhile, the self-assembly of colloids with SALR interactions confined in slit pores or cylinders has also been studied,[50–52] and the results suggest that helical structures are formed in systems confined in cylindrical pores,[51] similar to that in diblock copolymer systems.[30,47–49] Structures such as perpendicular lamellae, helices, embedded structures, perforated lamellar structures and concentric-spherical lamellae are predicted for diblock copolymers confined inside spherical cavities in theoretical and simulation studies.[30,38,39,43–46,53] SALR fluid on spherical surfaces and SALR colloids forming cylindrical structures within spherical shells have also been studied recently.[54,55] However, the self-assembly of colloids with SALR interactions confined in a spherical cavity is not fully understood yet.

In order to elucidate the similarities and differences between the self-assembly of SALR colloids and diblock copolymers under spherical confinement, in this paper we investigate the self-assembly of colloids with SALR interactions confined in spheres *via* molecular dynamics simulations. We compare the self-assembly behaviour between our confinement systems and bulk systems, as well as diblock copolymer systems. The differences in structures between spherically confined copolymer systems and bulk copolymer systems are solely due to the surface preference

School of Physics, Key Laboratory of Functional Polymer Materials of Ministry of Education, Nankai University, and Collaborative Innovation Center of Chemical Science and Engineering (Tianjin), Tianjin, 300071, China.
E-mail: liyao@nankai.edu.cn
† These authors contributed equally.

for a certain block.[30] In contrast, we reveal that the differences in structures between our systems and bulk colloidal systems are due to the bending of the confinement wall.

II. Model and methods

The interaction between colloidal particles is described using an effective SALR potential, which is the addition of a Lennard-Jones (LJ) potential plus a screened electrostatic interaction represented by the Yukawa potential (LJY):

$$u_{\mathrm{SALR}}(r_{ij}) = 4\varepsilon\left[\left(\frac{\sigma}{r_{ij}}\right)^{12} - \left(\frac{\sigma}{r_{ij}}\right)^{6}\right] + \frac{A}{(r_{ij}/\lambda)}\exp(-r_{ij}/\lambda) \quad (1)$$

where r_{ij} is the distance between particles i and j, and ε and σ are the usual LJ parameters. Parameter A measures the strength of the electrostatic interaction, and λ is the Debye screening length. The parameters are given the same values as in the bulk systems.[18] The potential function for $\varepsilon = 1.6$, $\sigma = 1.0$, $A = 0.65$ and $\lambda = 2.0$ is shown as the black curve in Fig. 1(a). In particular, we truncate the potential at $r_{\mathrm{cut}}/\sigma = 4.0$ to improve computational efficiency. In the following, we use σ and ε as the units of distance and energy respectively.

The confinement is imposed by placing a spherical wall with a radius of R_{w}. Particles interact with the wall *via* a truncated Lennard-Jones potential (WCA):[56]

$$u_{i\mathrm{w}}(r_{i\mathrm{w}}) = \begin{cases} 4\varepsilon_{\mathrm{w}}\left[\left(\frac{\sigma_{\mathrm{w}}}{r_{i\mathrm{w}}}\right)^{12} - \left(\frac{\sigma_{\mathrm{w}}}{r_{i\mathrm{w}}}\right)^{6}\right] + \varepsilon_{\mathrm{w}} & r_{i\mathrm{w}} < 2^{1/6}\sigma_{\mathrm{w}} \\ 0 & r_{i\mathrm{w}} \geq 2^{1/6}\sigma_{\mathrm{w}} \end{cases} \quad (2)$$

where $\varepsilon_{\mathrm{w}}/\varepsilon = 1.0$, $\sigma_{\mathrm{w}}/\sigma = 1.0$, and $r_{i\mathrm{w}}$ is the distance between particle i and the spherical wall R_{w}. The WCA potential between the particles and the spherical wall is shown as the red curve in Fig. 1(a). The total energy of this system is given by

$$u_{\mathrm{tot}} = \sum_{i=1}^{N-1}\sum_{j>i}^{N} u_{\mathrm{SALR}}(r_{ij}) + \sum_{i=1}^{N} u_{i\mathrm{w}}(r_{i\mathrm{w}}) \quad (3)$$

We employ molecular dynamics (MD) by using the open-source package LAMMPS.[57,58] We chose a confinement radius range of R/σ = 4–12 and a system density of 0.8 or less for our simulations. We employ the simulated annealing method to accelerate the equilibration of the systems and obtain the structures at low temperature.[59] The temperature is controlled by a Langevin thermostat with a relaxation time of 100dt, where the time step is $\mathrm{d}t = 0.005\sqrt{m\sigma^2/\varepsilon}$. The simulations are run for 10^7 time steps for equilibration at each temperature. The annealing process starts from the temperature $T^* = k_{\mathrm{B}}T/\varepsilon = 1.0$ to $T^* = 0.4$ with a temperature step of $\mathrm{d}T^* = 0.1$, and then continues from $T^* = 0.4$ to $T^* = 0.1$ with a temperature step of $\mathrm{d}T^* = 0.003$.

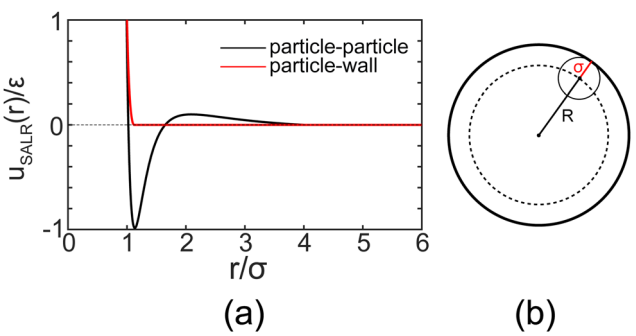

Fig. 1 Interaction function and illustration for free volume. (a) The LJY potential (eqn (1)) between a particle and another particle, and the WCA potential (eqn (2)) between a particle and the wall employed. (b) Illustration for free volume. The radius of the free volume of the particle centres is $R = R_{\mathrm{w}} - \sigma$, where R_{w} is the radius of the spherical wall.

The radius of the free volume for particles R is illustrated in Fig. 1(b). The number density is calculated based on free volume, which is defined as $\rho^* = \frac{N\sigma^3}{4\pi R^3/3}$. The radial density distribution $\rho_{\mathrm{r}}^*(r)$ is defined by

$$\rho_{\mathrm{r}}^*(r) = \frac{N(r, r+\Delta r)}{\frac{4}{3}\pi(r+\Delta r)^3 - \frac{4}{3}\pi r^3} \quad (4)$$

where $N(r,r+\Delta r)$ is the number of particles between r and $r+\Delta r$. We set $\Delta r = 0.1\sigma$ in our calculation. All plots of radial density distribution are averaged from 10 000 configurations, each of which is sampled every 100dt.

The various snapshots of the systems are plotted by the open-source visualisation software OVITO.[60] In order to clearly visualise the global structures, the alpha-shape method[61] and the Gaussian density method[62] are employed, which are surface mesh functions in OVITO.

The bond-orientation order parameters q_l and the hexatic order parameter Φ_6 for particles are calculated.[63,64] For each particle i, bond-orientation order parameter q_l is a real number defined as $q_l = \sqrt{\frac{4\pi}{2l+1}\sum_{m=-l}^{m=l}\bar{Y}_{lm}\bar{Y}_{lm}^*}$, where $\bar{Y}_{lm} = \frac{1}{N_{\mathrm{nn}}}\sum_{j=1}^{N_{\mathrm{nn}}} Y_{lm}(\theta(\boldsymbol{r}_{ij}), \phi(\boldsymbol{r}_{ij}))$. Here $Y_{lm}(\theta,\phi)$ are the spherical harmonics, bond vector $\boldsymbol{r}_{ij}$ is from particle i to one of its nearest neighbours, particle j, and N_{nn} is the number of nearest neighbours. We choose $l = 6$ and $l = 8$ in our calculation. The data of q_6 and q_8 are obtained using the LAMMPS compute command.

For each particle i in a 2D system, hexatic order parameter Φ_6 is defined as $\Phi_6 = \frac{1}{N_{\mathrm{nn}}}\sum_{j=1}^{N_{\mathrm{nn}}}\cos[6\theta(\boldsymbol{r}_{ij})]$, where N_{nn} is the number of nearest neighbours, bond vector $\boldsymbol{r}_{ij}$ is from particle i to one of its nearest neighbours, particle j, and the angle θ is formed by the bond vector $\boldsymbol{r}_{ij}$ and the given x axis. Though the systems we investigate are 3D, we calculate the Φ_6 of a particular particle by projecting the particle and its nearest neighbours in a spherical layer onto its tangent plane.

III. Results and discussions

The phase diagram is shown in Fig. 2. The density range we investigate is from 0 to 0.8, with a density separation $\Delta\rho^* <$ 0.02 between two adjacent simulated parameters. The systems

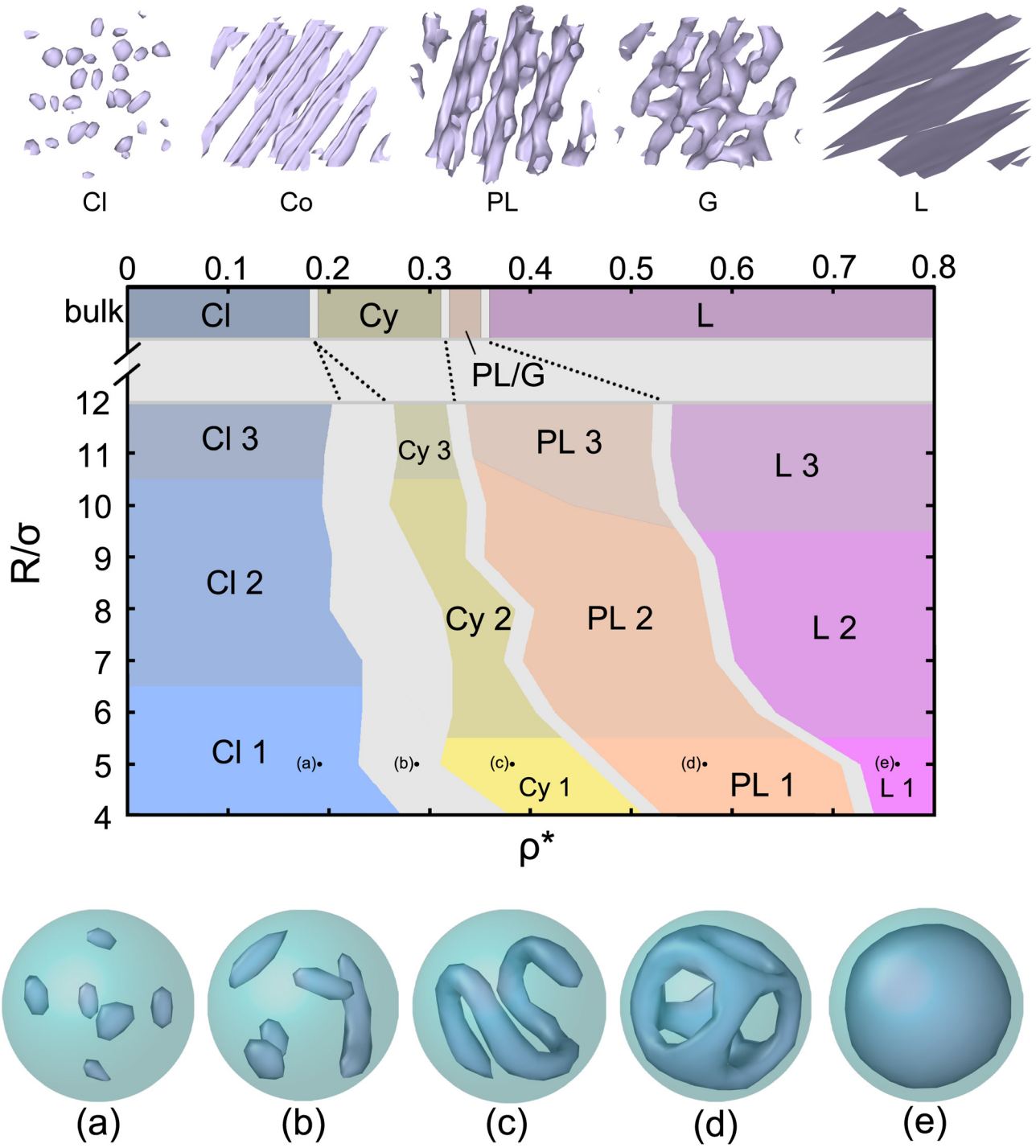

Fig. 2 Phase diagram and typical structures. Top row: Surfaces of each typical structure in bulk systems obtained by the alpha-shape method. The perforated lamellar (PL) structure and Gyroid (G) structure can occur under the same conditions when the density is appropriate. Mid panel: Phase diagram with the density and confinement radius as coordinates at $T^* = 0.1$, where different colours indicate different structures. The results of the bulk system are also shown. The phase behaviour shows four structures in order of increasing density: cluster (Cl), cylindrical (Cy), perforated lamellar (PL) and lamellar (L). The number of layers distributed radially increases with larger confinement radius, which is shown by the numbers in the diagram. The phase boundary lines are drawn in gray colour which represent the co-existence zone of the phases. All the phase boundaries roughly reflect the trend that the smaller the confinement radius is, the more to the right it is. Bottom row: Surfaces of each typical structure in the confinement system obtained by the alpha-shape method. Representative snapshots are taken with the parameters indicated by the solid dots in the phase diagram.

spontaneously form ordered structures at low temperature for the chosen parameters.

As density increases, we obtain four ordered structures of cluster, cylindrical, perforated lamellar and lamellar in turn.

The structure formed at each thermodynamic state is identified from surface snapshots. Spherelike clusters are identified as cluster structures. Long cylinders or rings with no or only one small cluster in the centre are identified as cylindrical structures. Concentric structures with three-fold or more than three-fold junctions are identified as perforated lamellar structures. We identify the structures as lamellar when there are no holes observed on the surface.

For the points near the phase boundary on the phase diagram, we performed 10 simulations, for the other points on the phase diagram, we performed 6 simulations. Points where the same structure consistently appears are identified as corresponding to that structure (*i.e.* the coloured regions in the phase diagram Fig. 2), while points where different structures emerge are identified as co-existence zones (*i.e.* the gray regions in the phase diagram shown in Fig. 2). We select the midpoint between two adjacent points representing different structures as the phase boundary on the phase diagram.

The phase boundaries generally tend to be at higher density with a smaller confinement radius. When we compare our systems with the bulk systems, we find that there is no wide co-existence zone from cluster to cylinder in the bulk systems. But there is a wide co-existence region between cluster structures and cylindrical structures in the phase diagram, where the mixture of clusters and short cylinders are observed. In bulk systems, the region of the perforated lamellar structures in the phase diagram is very narrow. The gyroid structures are observed in bulk systems. However, the gyroid structures are not observed in either colloidal systems or polymer systems under confinement.

Cluster

We show typical snapshots of cluster structures in Fig. 3(a) and (b). As the confinement radius of the system increases, the radial distribution of clusters form one-, two- and three-layer structures, which can be clearly recognized by the radial density distribution in Fig. 3(c).

We also find that the outermost clusters are arranged into vertices of regular Platonic solids (convex regular polyhedrons) at low temperatures in some cases (Fig. 4). This is very similar to diblock copolymer systems, and the packing of geometric solids under spherical confinement.[42,65] Among these polyhedrons, some are identified as *ortho*-tetrahedrons, *ortho*-octahedrons, *ortho*-icosahedrons, and others, as shown in Fig. 4. While in bulk systems, the cluster phase forms a lattice structure close to face-centred cubic (FCC) or body-centred cubic (BCC).[18]

We count the number and size of clusters from multiple simulations at each thermodynamic parameter. For all of our simulation results, no clusters with less than 13 particles are observed. When the density is $\rho^* = 0.18$, some big clusters emerge for it is close to the co-existence zone between cluster and cylinder. Though there are some big clusters with more than 30 particles, they are always very few. We notice that clusters with 13, 19, and 23 particles are usually the most common in our system. The shapes of clusters with 13 particles, 19 particles and 23 particles are regular, as shown in Fig. 5, which is the same as the results in the bulk system.[18]

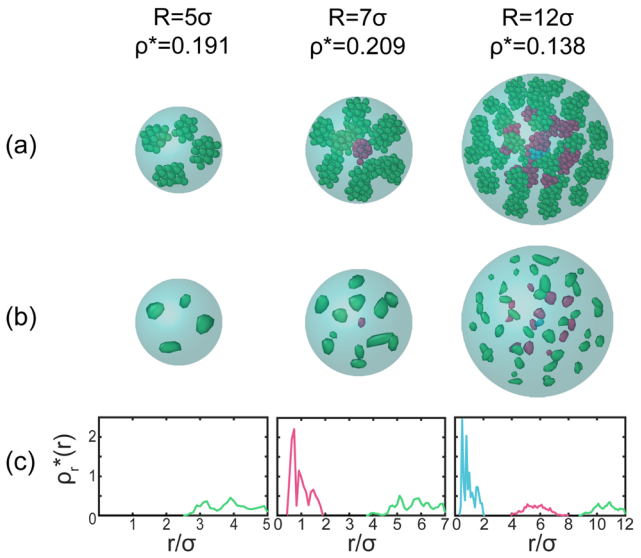

Fig. 3 Typical configurations and radial density distribution of the cluster structure. Snapshots are shown in (a) for the location of the particles and in (b) for the surfaces obtained by the alpha-shape method, with cluster structures formed under different parameters. (c) Radial density distribution for the corresponding cluster configurations, averaged from 10 000 configurations, each of which is sampled every 100dt. Snapshots and plots of the radial density distribution are colour-coded according to the radially distributed layer.

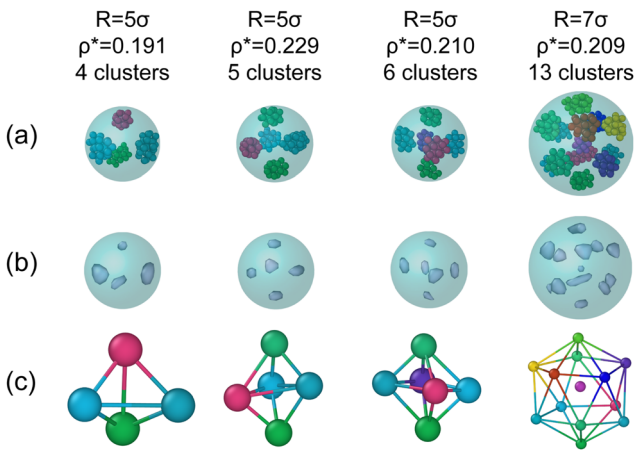

Fig. 4 Typical configurations of clusters arranged as the vertices of Platonic solids (or convex regular polyhedrons). From left to right is tetrahedron, double tetrahedron, octahedron, and icosahedron, respectively. Snapshots are shown in (a) for the locations of the particles and in (b) for the surfaces obtained by the alpha-shape method. Each sphere in (c) corresponds to the center of a cluster shown in (a).

Cylindrical

We show typical snapshots of cylindrical structures in Fig. 6(a) and (b). Clearly, the radial distribution of cylinders form one-, two- and three-layer structures as the confinement radius

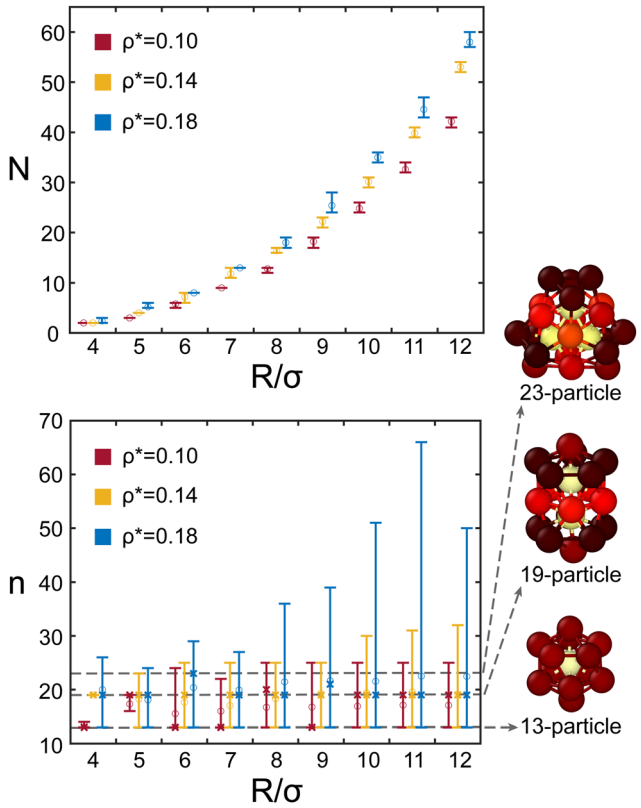

Fig. 5 Statistical fluctuation about the number and size of clusters formed. The top panel shows the minimum and maximum of the number of clusters formed, and the bottom panel shows the minimum and maximum of cluster size, in 3 different densities. The average value is shown by circles, and the mode for cluster size is shown by crosses. Three dashed lines in the bottom panel represent the mostly observed cluster sizes. Clusters with 13, 19, and 23 particles are mostly observed in our system, of which the shapes are shown at the right.

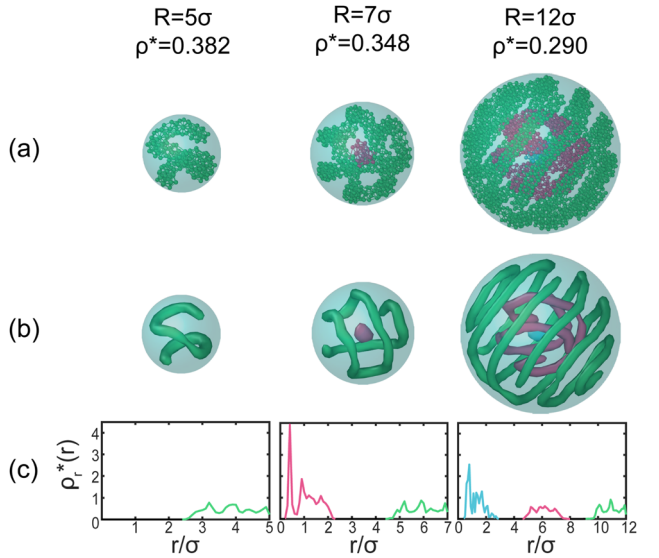

Fig. 6 Typical configurations and radial density distribution of the cylindrical structure. Snapshots are shown in (a) for the location of the particles with bonds added and in (b) for the surfaces obtained by the alpha-shape method, with cylindrical structures formed under different parameters. Bonds are added between the nearest neighbour particles in (a) for facilitating observation. (c) Radial density distribution for the corresponding configurations, averaged from 10 000 configurations, each of which is sampled every 100dt. Snapshots and plots of radial density distribution are colour-coded according to the radially distributed layer (the same as in Fig. 3).

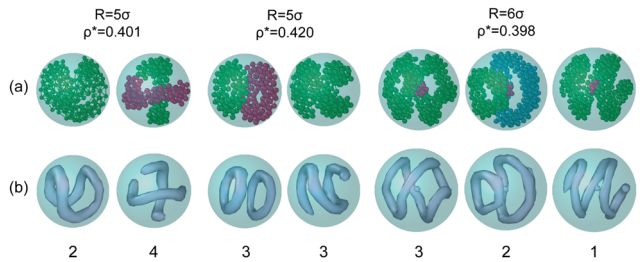

Fig. 7 Configurations of ring, saddle-shape and bent cylindrical structure. Snapshots are shown in (a) for the location of particles with bonds added and in (b) for the surfaces obtained by the alpha-shape method. There are three groups of snapshots, and snapshots in each group are taken under the same parameters with different random seeds in the simulation. The 1st and the 5th are saddle-shape structures. The 2nd, 4th and 7th are bent column structures. The 3rd and 6th are ring structures. Each number at the bottom row shows the occurrence frequency of a specific structure among 6 simulations.

increases, which can also be recognized by the radial density distribution in Fig. 6(c). The cylinders are curved along the spherical wall, which is different from bulk systems where the cylinders mostly maintain a straight shape.[18]

Multiple cylindrical structures can be obtained at the same thermodynamic state, which is similar to confined diblock copolymer systems.[42] Bent cylindrical structures, ring structures and saddle-shape structures can be formed, with snapshots shown in Fig. 7. We perform 6 simulations with different random seeds for each thermodynamic state. The average energy per particle is nearly equal for different cylindrical structures obtained at the same thermodynamic state. Examples include that the average energy per particle is around $(-1.48 \pm 0.03)\varepsilon$ when $R = 5\sigma$ and $\rho^* = 0.401$, around $(-1.45 \pm 0.03)\varepsilon$ when $R = 5\sigma$ and $\rho^* = 0.420$, and around $(-1.41 \pm 0.03)\varepsilon$ when $R = 6\sigma$ and $\rho^* = 0.398$. Different cylindrical structures are obtained at different frequencies in different thermodynamic states. Configurations and occurrence frequencies of frequent structures at some specific thermodynamic states are shown in Fig. 7. The morphology of the saddle-shape structure is similar to the semiflexible ring polymers under spherical confinement.[66] As the density increases, the saddle-shape ring might bend further, or form multiple rings, or become longer cylinders (Fig. 7).

When the density is between the density of forming the cluster and cylindrical structures, mixture structures of clusters and cylinders are formed, with typical snapshots shown in Fig. 8(a) and (b). It corresponds to the structures in the wide co-existence region of clusters and cylinders in the phase diagram. The radial distribution of mixtures forms one-, two- and three-layer structures as the confinement radius increases,

which is the same as previously discussed in cluster structures and cylindrical structures. The radial density distribution is plotted in Fig. 8(c).

Perforated lamellar

With a density larger than that of forming the cylindrical structures, perforated lamellar structures are formed. Typical snapshots are shown in Fig. 9(a) and (b). As the density increases, the cylinders are connected to each other. These structures are similar to the structures of diblock copolymers confined in spheres.[39,41] Clearly, systems exhibit multi-layer structures as the wall radius gradually increases, which can also be recognized by the radial density distribution shown in Fig. 9(c). We note that at $R = 9\sigma$ and $\rho^* = 0.426$, the system is a two-layer structure (Fig. 9(d)). Both the outer layer and the inner layer are perforated lamellar structures. While at $R = 12\sigma$ and $\rho^* = 0.345$, the innermost particles form a cluster (Fig. 9(e)).

Lamellar

When the systems are denser, lamellar structures are formed. The lamellae crystallise at low temperatures (as shown in Fig. 10(a and b) and 11), which is not observed in confined diblock copolymer systems.[30] According to the plots shown in Fig. 12, when the temperature is over $T^* = 0.4$, the order parameter Φ_6 is nearly 0 and q_6 and q_8 are also small, which suggests that the system is disordered at high temperatures. The order parameters Φ_6, q_6 and q_8 significantly increase at low temperatures, meaning that systems become ordered and the lamellae crystallise except for unavoidable defects. The local shape of the spherical lamella is nearly flat to form an energetically favourable structure (Fig. 10(b)). Similar to experimental and simulated results involving other colloids or hard geometric solids, crystallised lamellae form *ortho*-icosahedrons.[67–71] We can see that there are obvious patterns of defects, satisfying the topologic requirement.

In bulk systems, the lamellar structure behaves as flat lamellae parallel to each other.[18] In our systems, the particles form a concentric spherical lamellar structure, which is also observed in spherically confined diblock copolymer systems.[30,39] As the wall radius increases, the system gradually exhibits a multilayer structure (Fig. 10(c)). Each layer will form the same lamellar structure when the density and the confinement radius is appropriate. The thickness of each lamella is 2 or 3 particles, as shown in the snapshots in Fig. 10(c) and the radial density distribution in Fig. 10(d). The thickness of each spherical lamella is not fixed. It is influenced by the size and density.

The phase boundaries generally tend to be at greater density with smaller wall radius (Fig. 2). We proposed the mechanism

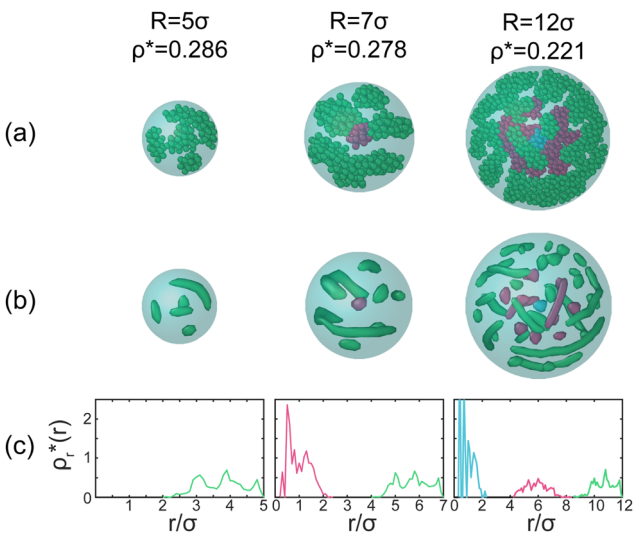

Fig. 8 Typical configurations and radial distribution of the mixture structure of clusters and cylinders. Snapshots are shown in (a) for the location of the particles and in (b) for the surfaces obtained by the alpha-shape method, with mixture structures formed under different parameters. (c) Radial density distribution for the corresponding configurations (truncated at $\rho_r^*(r) = 2.5$), averaged from 10 000 configurations, each of which is sampled every 100dt. Snapshots and plots of radial density distribution are colour-coded according to the radially distributed layer (the same as in previous figures).

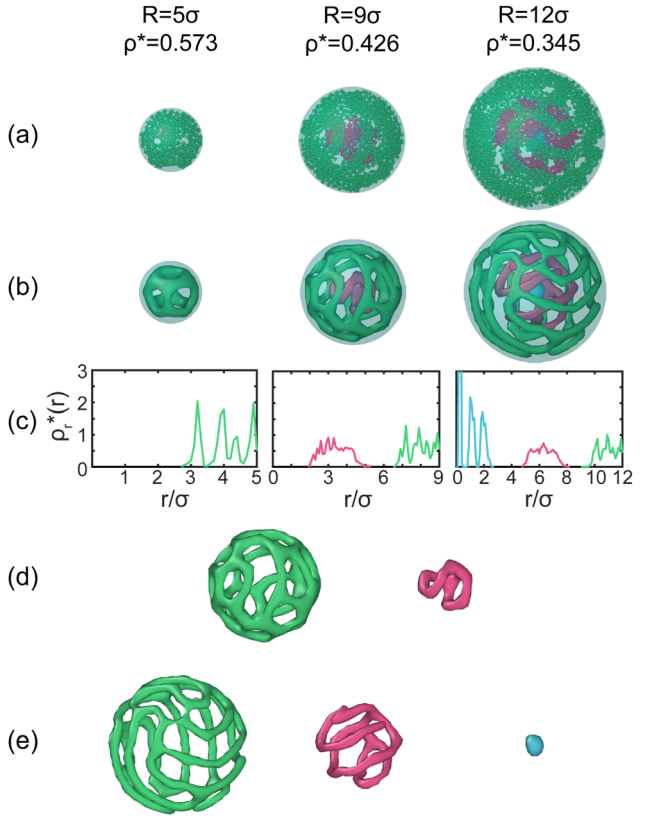

Fig. 9 Typical configurations and radial density distribution of the perforated lamellar structure. Snapshots are shown in (a) for the location of the particles with bonds added and in (b) for the surfaces obtained by the alpha-shape method. (c) Radial density distribution for the corresponding configurations (truncated at $\rho_r^*(r) = 3$), averaged from 10 000 configurations, each of which is sampled every 100dt. (d) Separated snapshots of surfaces when $R = 9\sigma$ and $\rho^* = 0.426$. Each layer shows a similar perforated lamellar structure. (e) Separated snapshots of surfaces when $R = 12\sigma$ and $\rho^* = 0.345$. The innermost particles form a cluster. Snapshots and plots of radial density distribution are colour-coded according to the radially distributed layer (the same as in previous figures).

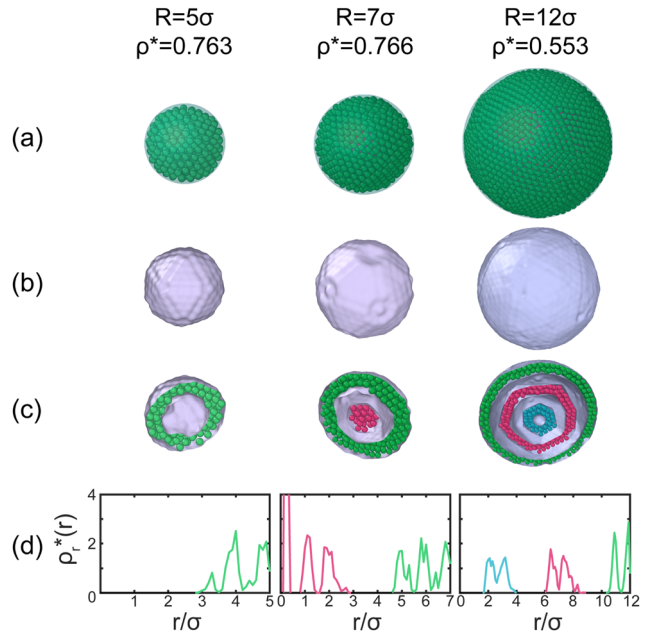

Fig. 10 Typical configurations and radial density distribution of the lamellar structure. Snapshots are shown in (a) for the location of the particles and in (b) for the surfaces obtained by the Gaussian density method. (c) Sliced snapshots for the corresponding configurations in (b). (d) Radial density distribution for the corresponding configurations (truncated at $\rho_r^*(r) = 4$), averaged from 10 000 configurations, each of which is sampled every 100dt. Snapshots and plots of radial density distribution are colour-coded according to the radially distributed layer (the same as in previous figures).

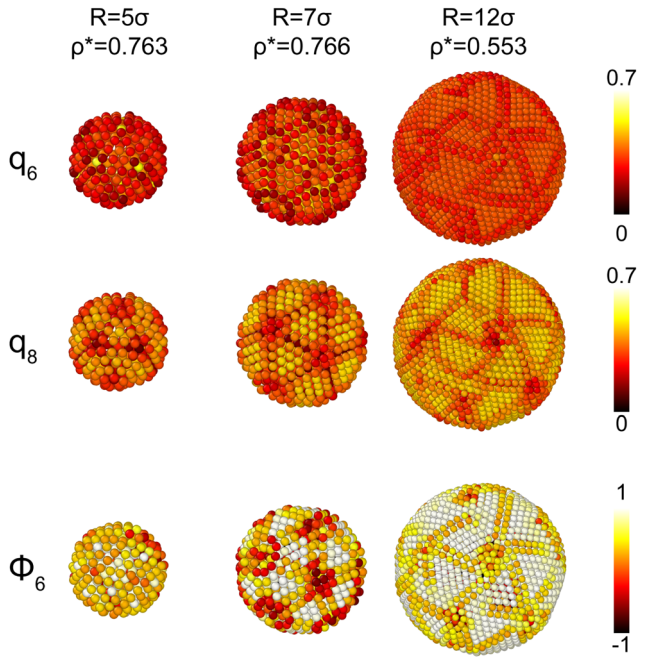

Fig. 11 Snapshots of the lamellar structure colour-coded according to the order parameters. The top and mid rows are according to q_6 and q_8 respectively, with the colour bar range from 0 to 0.7. The bottom row is according to Φ_6 order, with the colour bar ranging from −1 to 1. The high order parameters indicate most parts of the layers are crystallised except those unavoidable defects.

for explaining this phenomenon, with an illustration shown in Fig. 13. The layer composed of particles is flat in bulk systems, while it will bend when it is confined in a spherical wall. As the layer bends along with the spherical wall, some particles in region III in Fig. 13 enter region II, increasing the average energy per particle. Particles entering region II will be attracted by the shaded particle into the lower-energy region I, or be repelled to the lower-energy truncated region III, therefore the layer will be thicker and more perforated, reducing the additional positive potential energy. Consequently, more perforated lamellar structures are formed at the density where lamellar structures are formed in bulk systems. Concretely, when the density is $\rho^* = 0.380$, a lamellar structure is formed in the bulk system, while a perforated lamellar structure is formed when it was confined in a sphere with $R = 12\sigma$ (Fig. 14(a)–(c)). Due to the same reason, colloids confined in spheres tend to form more cylindrical structures at the density where perforated lamellar structures are formed in bulk systems.

Furthermore, the smaller the wall radius is, the greater the curvature of the lamella becomes, which means that more particles enter region II, resulting in a greater increase in average energy per particle. Thus, the system is energetically more favourable for forming a perforated structure when the confinement radius is smaller, which results in the phase boundaries tilting to the right.

Our simulations show that colloidal systems under spherical confinement tend to form more perforated lamellar structures than colloidal systems in bulk (Fig. 14(a)–(c)). Though our systems form perforated lamellar structures with a smaller outer surface, the perforated lamella is thicker than the lamellae in bulk (which can be clearly recognised by the density distribution shown in Fig. 14(d)), suggesting that the number of particles in one layer is almost unchanged. Also, the structure of each layer is almost the same. This suggests that, compared with the bulk system, when a layer in a confinement system become bent, the particles at the layer relocate within the same layer as shown in Fig. 13 and form more perforated and thicker structures, rather than relocating to another layer.

In terms of lamellae in bulk systems, the distance between lamellae is between 3σ and 4σ (see the blue curve in Fig. 14(d)). This means that different particles at different lamellae interact with each other at the end of the repulsive region with very small potential energy, or in the cut-off region (see the potential function in Fig. 1(a)). If more perforated and thicker lamellar structures are formed in the bulk system, the distance between different lamellae become closer, around 2.5σ, and more particles will interact in the repulsive region with greater potential energy. These particles obtain much greater positive potential energy from interlayer interaction, thus it is not energetically favourable to form perforated structures in bulk. However, as previously discussed, forming perforated and thicker structures can reduce the additional intralayer potential energy in confinement systems. The reduction of intralayer energy is greater than the increase of interlayer energy brought by becoming thicker. This competition between interlayer energy

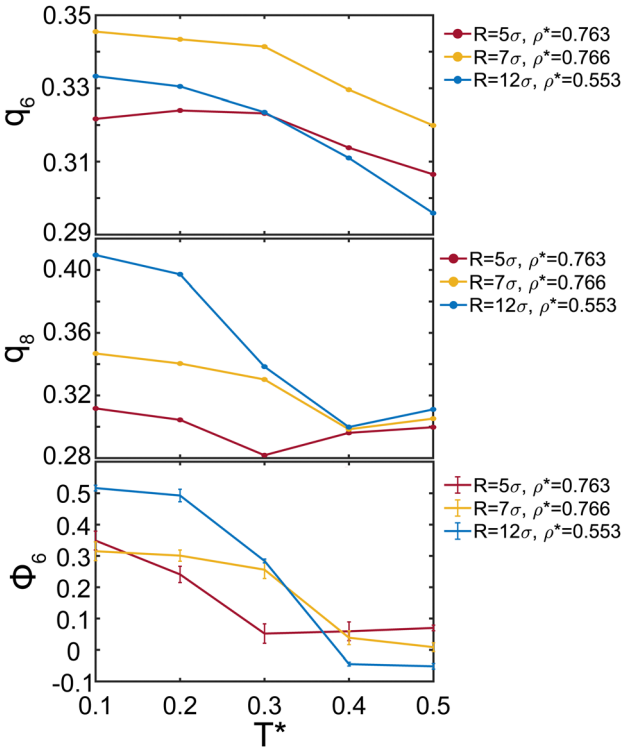

Fig. 12 Three structure order parameters as functions of temperature T^*, for 3 different confined radii and densities in Fig. 10 and 11. The top shows q_6 order, the mid shows q_8 order, and the bottom shows Φ_6 order. The error bars (minimum and maximum) of Φ_6 are shown in the plot. The sizes of error bars (minimum and maximum) of q_6 and q_8 are smaller than the size of the data dots.

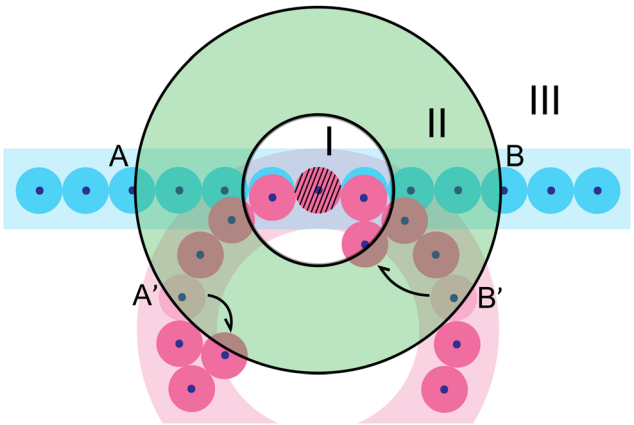

Fig. 13 Illustration for the mechanism of bending. This figure is a sliced illustration for 3D systems. The thickness of each lamella is 2 or 3 particles, which is illustrated by the light blue and light red area. Roughly, the blue circles represent particles of a straight lamella in bulk systems, while the red circles represent particles of a bending lamella in spherical confinement systems. Particles A and A′, and B and B′ represent the same particle in bulk and under spherical confinement respectively. The green-coloured region II represents the spherical-shell-shape space of positive potential energy, while the part inside (region I) represents the space of negative potential energy, given by the shaded particle at the centre. The shaded particle does not interact with outside particles (region III). As the flat lamella bends along with the spherical wall, some particles enter region II from region III (*e.g.* particles A′ and B′), increasing the average energy per particle. These particles will be repelled to region III like particle A′, or be attracted to region I like particle B′, for reducing the additional potential energy, which makes the lamella perforated.

and intralayer energy results in more perforation under confinement but less perforation in bulk.

The confinement wall we use is neutral and only has volume exclusion. Colloids confined in spheres form more perforated structures than in bulk, while the diblock copolymers confined in neutral spherical walls are not obviously perforated compared with in bulk.[30] The reason for this difference is that there is not a mechanism of bending in confined diblock copolymer systems. In confined diblock copolymer systems, the interaction between the wall and the block dominates, and blocks tend to relocate themselves among different layers. The self-assembly structures are significantly different according to the wall surface preference for the block.[30,39]

We measure the average energy per particle for densities $\rho^* = 0.15$, 0.30, 0.45 and 0.60, at $T^* = 0.1$ for different confinement radii. At the same density, the average energy per particle in our systems is below that in bulk systems, which is shown in Fig. 15. The explanation for this phenomenon is illustrated in Fig. 16. In both bulk and confinement systems, the distance between lamellae (or cylinders, or clusters) remains around 3σ (see *e.g.* Fig. 14(d)). Particles at this distance repel each other with a positive potential energy. As a result, there is a positive potential energy between the outer particles and the inner particles. In spherical confinement systems, the energy given by the outside of the outermost particles vanished

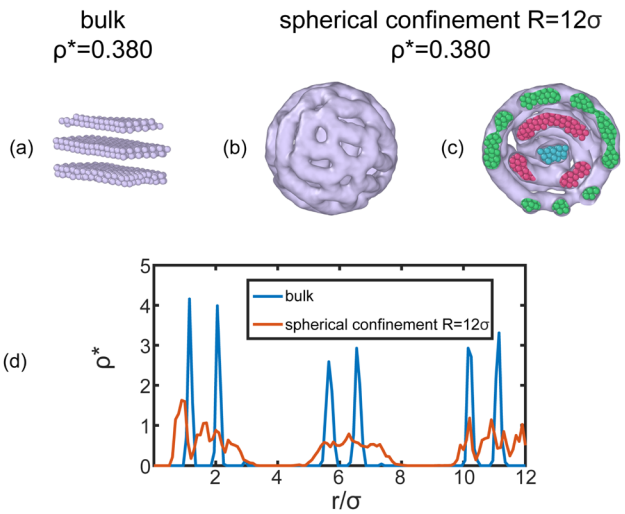

Fig. 14 Comparison between the bulk system and the spherical confinement system with the same density at $\rho^* = 0.380$. (a) Snapshot of the bulk system showing the location of the particles, with a lamellar structure formed. (b) Surfaces of the spherical confinement system with $R = 12\sigma$ obtained by the Gaussian density method, with a perforated lamellar structure formed. (c) Sliced snapshot of (b). (d) Density distribution of the bulk system (along the direction perpendicular to the lamellae), and radial density distribution of the system under confinement, averaged from 1000 configurations, each of which is sampled every 100d*t*.

(Fig. 16 right column), resulting in a decrease in average energy per particle compared with the bulk systems (Fig. 16 left

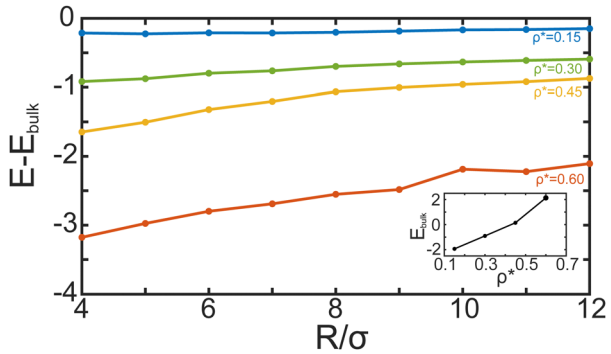

Fig. 15 Difference of the average energy per particle between the bulk system and the spherical confinement system. The solid blue, green, yellow and orange curves are the average energy per particle in confinement systems of different confinement radii minus that in the bulk system, for densities ρ^* = 0.15, 0.30, 0.45, and 0.60 respectively. The inserted figure is a plot of energy *versus* density in the bulk system. The fluctuation of the energy is smaller than the solid dots in the plot.

Fig. 16 Illustration for the decrease in energy brought by confinement. This is merely an illustration, and the dots in the figure do not refer to any specific structures. Each coloured ring represents a lamella with a thickness of 2 or 3 particles. Left: Illustration of the bulk system. There is a positive potential energy ΔE between the outer particles and the more outer particles. As the radius goes to infinity, the spherical layer becomes a flat layer. The case of a bulk system will be equivalent to the case of this illustration. Right: Illustration of the confinement system. With the addition of the spherical confinement wall, there are no more outer particles in the system and therefore no positive potential energy ΔE.

column). At the same time, the smaller the confinement radius is, the larger the ratio of the surface particle number to the number of all particles becomes. Therefore, more energy given by outside particles vanishes under smaller confinement radius. This causes the energy diagram to reflect a trend where the smaller the wall radius is, the smaller the average energy per particle of the system is.

The confinement causes additional positive energy generated by the bending of the layer. But the vanished energy is significantly greater than the additional energy brought by bending. Therefore, the overall average energy per particle for our confinement systems is smaller than that for the bulk systems.

IV. Conclusion

In this article we have studied colloidal systems with competing interactions confined in spheres. Our results showed that, in spherical confinement systems of particles with SALR interactions, the cluster, cylindrical, perforated lamellar, and lamellar structures are formed at low temperature. The configuration of self-assembled clusters in some cases fits the vertices of Platonic solids. More structures such as ring structures are formed under confinements compared with the bulk systems.[18] We also found that the average energy per particle is below that in bulk systems. Crystallisation occurs on the surface at appropriate densities, which is not observed in diblock copolymer systems.[30,39]

Moreover, we found that the phase boundaries tend to be at higher density with smaller confinement radius. Our systems tend to form perforated structures when confined in smaller spheres, which is different from diblock copolymer systems.[30] Perforated lamellar structures are formed in spherical confinement systems at densities where lamellar structures are formed in the bulk systems. Layers composed of particles bend along the wall in confined SALR colloidal systems, which increases the average energy per particle. Perforated lamellar structures are energetically favourable under spherical confinement. Due to the same reason, column structures are formed at densities where perforated lamellar structures are formed in the bulk systems. However, in confined diblock copolymer systems, the differences of structures compared with the bulk systems are almost only due to the interaction between the wall and the block.[30] The intralayer relocation of the colloidal particles causes the layer to become perforated and thicker, while similar structural changes in polymer systems only caused by interlayer relocation. The mechanism of structural changes in colloidal systems under spherical confinement is completely different from that in copolymer systems. The studies on SALR fluid on spherical surfaces and SALR colloids in spherical shells focused on quasi-two-dimensional systems, characterized by a single layer of particles.[54,55] In these single-layer systems, it is impossible to investigate the phenomenon about multiple layers, for example the competition between interlayer energy and intralayer energy results in more perforated lamellar structure formation in the current work.

We hope this study helps in the design of particle self-assembly under confinement especially the utility of the curvature of the confinement wall, with promising applications in nanostructure designs and understanding living systems, such as porous structure formations.

Author contributions

Conceptualisation, Y. L.; methodology, N. L. and J. L.; validation, N. L. and J. L.; formal analysis, N. L., J. L., and Y. L.; investigation, N. L., J. L., and Y. L.; data curation, N. L. and J. L.; writing – original draft, N. L., J. L.; writing – review and editing, N. L., J. L., L. Q., S. M., Y. L., B. L.; visualisation, N. L. and J. L.; supervision, B. L. and Y. L.; project administration, B. L. and Y. L.; funding acquisition, B. L. and Y. L.

Conflicts of interest

There are no conflicts to declare.

Acknowledgements

This work was supported by the National Natural Science Foundation of China (12275137), the Nankai University Undergraduate Innovative Research Program, and the Fundamental Research Funds for the Central Universities, Nankai University (63221053, 63231190). We thank Ho-Kei Chan and Peng Tan for the helpful discussions, and Jun Zhong for helping with data visualisation.

References

1 D. Philp and J. F. Stoddart, *Angew. Chem., Int. Ed. Engl.*, 1996, **35**, 1154–1196.
2 G. Whitesides and B. Grzybowski, *Science*, 2002, **295**, 2418–2421.
3 H. Hu, M. Gopinadhan and C. O. Osuji, *Soft Matter*, 2014, **10**, 3867.
4 G. S. Doerk and K. G. Yager, *Mol. Syst. Des. Eng.*, 2017, **2**, 518–538.
5 H. Míguez, S. M. Yang and G. A. Ozin, *Langmuir*, 2003, **19**, 3479–3485.
6 C. P. Royall, *Soft Matter*, 2018, **14**, 4020–4028.
7 J. Ruiz-Franco and E. Zaccarelli, *Annu. Rev. Condens. Matter Phys.*, 2021, **12**, 51–70.
8 A. Al Harraq, A. A. Hymel, E. Lin, T. M. Truskett and B. Bharti, *Commun. Chem.*, 2022, **5**, 72.
9 H. M. Gauri, Z. M. Sherman, A. Al Harraq, T. M. Truskett and B. Bharti, *Soft Matter*, 2023, **19**, 4439–4448.
10 A. Stradner, H. Sedgwick, F. Cardinaux, W. Poon, S. Egelhaaf and P. Schurtenberger, *Nature*, 2004, **432**, 492–495.
11 H. Sedgwick, J. E. Cameron, W. C. K. Poon and S. U. Egelhaaf, *J. Chem. Phys.*, 2007, **127**, 125102.
12 A. I. Campbell, V. J. Anderson, J. S. van Duijneveldt and P. Bartlett, *Phys. Rev. Lett.*, 2005, **94**, 208301.
13 R. Sanchez and P. Bartlett, *J. Phys.: Condens. Matter*, 2005, **17**, S3551.
14 C. L. Klix, C. P. Royall and H. Tanaka, *Phys. Rev. Lett.*, 2010, **104**, 165702.
15 M. Kohl, R. Capellmann, M. Laurati, S. Egelhaaf and M. Schmiedeberg, *Nat. Commun.*, 2016, **7**, 11817.
16 D. Pini and A. Parola, *Soft Matter*, 2017, **13**, 9259–9272.
17 Y. Zhuang, K. Zhang and P. Charbonneau, *Phys. Rev. Lett.*, 2016, **116**, 098301.
18 H. Serna, A. D. Pozuelo, E. G. Noya and W. T. Góźdź, *Soft Matter*, 2021, **17**, 4957–4968.
19 H. J. Zhao, V. R. Misko and F. M. Peeters, *New J. Phys.*, 2012, **14**, 063032.
20 B. Yu, B. Li, P. Sun, T. Chen, Q. Jin, D. Ding and A.-C. Shi, *J. Chem. Phys.*, 2005, **123**, 234902.
21 F. S. Bates, M. F. Schulz, A. K. Khandpur, S. Förster, J. H. Rosedale, K. Almdal and K. Mortensen, *Faraday Discuss.*, 1994, **98**, 7–18.
22 M. W. Matsen and M. Schick, *Phys. Rev. Lett.*, 1994, **72**, 2660–2663.
23 M. W. Matsen and F. S. Bates, *Macromolecules*, 1996, **29**, 1091–1098.
24 D. A. Hajduk, H. Takenouchi, M. A. Hillmyer, F. S. Bates, M. E. Vigild and K. Almdal, *Macromolecules*, 1997, **30**, 3788–3795.
25 O. N. Vassiliev and M. W. Matsen, *J. Chem. Phys.*, 2003, **118**, 7700–7713.
26 M. W. Matsen, G. H. Griffiths, R. A. Wickham and O. N. Vassiliev, *J. Chem. Phys.*, 2006, **124**, 024904.
27 A. Ciach, J. Pe kalski and W. T. Góźdź, *Soft Matter*, 2013, **9**, 6301.
28 S. Park, H. Hwang, M. Kim, J. H. Moon and S.-H. Kim, *Nanoscale*, 2020, **12**, 18576–18594.
29 H. Yabu, T. Higuchi and H. Jinnai, *Soft Matter*, 2014, **10**, 2919–2931.
30 A.-C. Shi and B. Li, *Soft Matter*, 2013, **9**, 1398–1413.
31 C. R. Stewart-Sloan and E. L. Thomas, *Eur. Polym. J.*, 2011, **47**, 630–646.
32 Y. Yin, P. Sun, T. Chen, B. Li, Q. Jin, D. Ding and A.-C. Shi, *ChemPhysChem*, 2004, **5**, 540–548.
33 P. Chen, H. Liang and A.-C. Shi, *Macromolecules*, 2007, **40**, 7329–7335.
34 B. Yu, P. Sun, T. Chen, Q. Jin, D. Ding, B. Li and A.-C. Shi, *J. Chem. Phys.*, 2007, **127**, 114906.
35 B. Yu, P. Sun, T. Chen, Q. Jin, D. Ding, B. Li and A.-C. Shi, *J. Chem. Phys.*, 2007, **126**, 204903.
36 B. Yu, P. Sun, T. Chen, Q. Jin, D. Ding, B. Li and A.-C. Shi, *Phys. Rev. Lett.*, 2006, **96**, 138306.
37 B. Yu, Q. Jin, D. Ding, B. Li and A.-C. Shi, *Macromolecules*, 2008, **41**, 4042–4054.
38 P. Chen, H. Liang and A.-C. Shi, *Macromolecules*, 2008, **41**, 8938–8943.
39 B. Yu, B. Li, Q. Jin, D. Ding and A.-C. Shi, *Macromolecules*, 2007, **40**, 9133–9142.
40 F. Zhao, Z. Xu and W. Li, *Macromolecules*, 2021, **54**, 11351–11359.
41 W. Li and R. A. Wickham, *Macromolecules*, 2009, **42**, 7530–7536.
42 J. Wu, X. Wang, Z. Wang, Y. Yin, R. Jiang, Y. Li and B. Li, *Macromolecules*, 2023, **56**, 335–348.
43 B. Yu, B. Li, Q. Jin, D. Ding and A.-C. Shi, *Soft Matter*, 2011, **7**, 10227–10240.
44 P. Chi, Z. Wang, B. Li and A.-C. Shi, *Langmuir*, 2011, **27**, 11683–11689.
45 J. G. E. M. Fraaije and G. J. A. Sevink, *Macromolecules*, 2003, **36**, 7891–7893.
46 J. Huh, C. Park and Y. K. Kwon, *J. Chem. Phys.*, 2010, **133**, 114903.
47 P. Chen, X. He and H. Liang, *J. Chem. Phys.*, 2006, **124**, 104906.
48 J. Feng and E. Ruckenstein, *J. Chem. Phys.*, 2006, **125**, 164911.
49 M. Pinna, X. Guo and A. V. Zvelindovsky, *J. Chem. Phys.*, 2009, **131**, 214902.
50 H. Serna, W. T. Góźdź and E. G. Noya, *Int. J. Mol. Sci.*, 2021, **22**, 11050.

51 H. Serna, E. G. Noya and W. T. Góźdź, *Langmuir*, 2019, **35**, 702–708.
52 S. Franzini, L. Reatto and D. Pini, *Soft Matter*, 2018, **14**, 8724–8739.
53 S. Li, P. Chen, L. Zhang and H. Liang, *Langmuir*, 2011, **27**, 5081–5089.
54 S. Franzini, L. Reatto and D. Pini, *Soft Matter*, 2022, **18**, 186–197.
55 H. Serna, A. G. Meyra, E. G. Noya and W. T. Gózdz, *Soft Matter*, 2023, **19**, 5103–5117.
56 H. C. Andersen, J. D. Weeks and D. Chandler, *Phys. Rev. A: At., Mol., Opt. Phys.*, 1971, **4**, 1597–1607.
57 S. Plimpton, *J. Comput. Phys.*, 1995, **117**, 1–19.
58 A. P. Thompson, H. M. Aktulga, R. Berger, D. S. Bolintineanu, W. M. Brown, P. S. Crozier, P. J. in 't Veld, A. Kohlmeyer, S. G. Moore, T. D. Nguyen, R. Shan, M. J. Stevens, J. Tranchida, C. Trott and S. J. Plimpton, *Comput. Phys. Commun.*, 2022, **271**, 108171.
59 S. Kirkpatrick, C. Gelatt and M. Vecchi, *Science*, 1983, **220**, 671–680.
60 A. Stukowski, *Modell. Simul. Mater. Sci. Eng.*, 2010, **18**, 015012.
61 A. Stukowski, *JOM*, 2013, **66**, 399.
62 M. Krone, J. Stone, T. Ertl and K. Schulten, EuroVis – Short Papers, 2012.
63 P. J. Steinhardt, D. R. Nelson and M. Ronchetti, *Phys. Rev. B: Condens. Matter Mater. Phys.*, 1983, **28**, 784–805.
64 D. R. Nelson and B. I. Halperin, *Phys. Rev. B: Condens. Matter Mater. Phys.*, 1979, **19**, 2457–2484.
65 E. G. Teich, G. van Anders, D. Klotsa, J. Dshemuchadse and S. C. Glotzer, *Proc. Natl. Acad. Sci. U. S. A.*, 2016, **113**, E669–E678.
66 J. Guven and P. Vázquez-Montejo, *Phys. Rev. E: Stat., Nonlinear, Soft Matter Phys.*, 2012, **85**, 026603.
67 J. Wang, C. F. Mbah, T. Przybilla, B. Apeleo Zubiri, E. Spiecker, M. Engel and N. Vogel, *Nat. Commun.*, 2018, **9**, 5259.
68 J. Wang, C. F. Mbah, T. Przybilla, S. Englisch, E. Spiecker, M. Engel and N. Vogel, *ACS Nano*, 2019, **13**, 9005–9015.
69 D. Wang, T. Dasgupta, E. B. van der Wee, D. Zanaga, T. Altantzis, Y. Wu, G. M. Coli, C. B. Murray, S. Bals, M. Dijkstra and A. van Blaaderen, *Nat. Phys.*, 2021, **17**, 128–134.
70 Y. Chen, Z. Yao, S. Tang, H. Tong, T. Yanagishima, H. Tanaka and P. Tan, *Nat. Phys.*, 2021, **17**, 121–127.
71 D. Wang, M. Hermes, R. Kotni, Y. Wu, N. Tasios, Y. Liu, B. de Nijs, E. B. van der Wee, C. B. Murray, M. Dijkstra and A. van Blaaderen, *Nat. Commun.*, 2018, **9**, 2228.